

# Direct Observation of Ferroelectric Domain Walls in $\text{LiNbO}_3$ : Wall-Meanders, Kinks, and Local Electric Charges

Julie Gonnissen, Dmitry Batuk, Guillaume F. Nataf, Lewys Jones, Artem M. Abakumov, Sandra Van Aert, Dominique Schryvers,\* and Ekhard K. H. Salje

Direct observations of the ferroelectric domain boundaries in  $\text{LiNbO}_3$  are performed using high-resolution high-angle annular dark field scanning transmission electron microscopy imaging, revealing a very narrow width of the domain wall between the  $180^\circ$  domains. The domain walls demonstrate local side-way meandering, which results in inclinations even when the overall wall orientation follows the ferroelectric polarization. These local meanders contain kinks with “head-to-head” and “tail-to-tail” dipolar configurations and are therefore locally charged. The charged meanders are confined to a few cation layers along the polarization direction and are separated by longer stretches of straight domain walls.

## 1. Introduction

Ferroic domain walls can be functional elements of a material while the same functionality does not exist in the bulk.<sup>[1]</sup> Typical examples are conducting domain walls in  $\text{BiFeO}_3$ ,<sup>[2–4]</sup>  $\text{Pb}(\text{Zr,Ti})\text{O}_3$ ,<sup>[5]</sup> superconducting twin walls in  $\text{WO}_3$ ,<sup>[6,7]</sup> polarity and ferroelectricity in ferroelastic domain walls in  $\text{CaTiO}_3$  and

$\text{SrTiO}_3$ ,<sup>[8–11]</sup> and segregation of chemical species in domain walls.<sup>[1,12]</sup> Direct structural observations of displacements inside domain walls are rare, however.<sup>[9,13,14]</sup> It is even harder to show fine structures, such as additional symmetry breaking, inside domain walls. The only reported case is the polarity in twin walls in  $\text{CaTiO}_3$  revealed by high resolution transmission electron microscopy observations.<sup>[9]</sup>

Ferroelectric walls in  $\text{LiNbO}_3$  are expected to display transport functionality: the walls are locally electrically charged, while the bulk is known not to contain any electric charges besides those related

to point defects. These walls are expected to be electrically conducting when the carrier concentration is sufficiently large.<sup>[15–18]</sup> Ferroelectric walls in  $\text{LiNbO}_3$  separate domains with the polarizations pointing in opposite directions ( $180^\circ$  walls). The geometrical condition for charged walls is that they are inclined with respect to the equilibrium direction along the ferroelectric polarization direction [0001] (in the hexagonal setting).<sup>[15–17]</sup>

Such inclined and conductive walls have previously been observed in  $\text{Pb}(\text{Zr,Ti})\text{O}_3$  thin films<sup>[19]</sup> and calculations demonstrate that the static conductivity drastically increases at inclined domain walls, even for small inclination angles.<sup>[18]</sup> Electron microscopy has shown that charged domain walls, particularly in the most extreme case of a head-to-head or tail-to-tail configuration, act as barriers for defect movements.<sup>[20–26]</sup> Inclined walls generate local strain in the nearby bulk, while walls in mechanical equilibrium are neither charged nor do they strain the lattice. However,  $\text{LiNbO}_3$  with macroscopically noninclined walls still contains significant defect structures<sup>[20,27–29]</sup> which decorate the walls.<sup>[30,31]</sup> Nataf et al. argued that even “straight” walls should show local inclinations, they “meander,” so that head-to-head and tail-to-tail dipolar kink configurations occur locally.<sup>[24]</sup> Each such configuration represents an increase or decrease of carrier concentrations and hence corresponds to a local charge monopole.

$\text{LiNbO}_3$  has a trigonal structure with the  $R\bar{3}c$  space group in the paraelectric phase. With the onset of ferroelectricity at  $T_c$  near 1483 K, the structure remains trigonal, but the inversion symmetry of the system is lifted, reducing the symmetry to the  $R3c$  space group.  $\text{LiNbO}_3$  is hence ferroelectric but not ferroelastic below 1483 K. Domain structures consist exclusively of  $180^\circ$  ferroelectric walls, which are almost strain-free in thermodynamic equilibrium while weak local strains originate from coupling between the polarization and secondary

J. Gonnissen, Dr. D. Batuk, Prof. A. M. Abakumov, Prof. S. Van Aert, Prof. D. Schryvers  
Electron Microscopy for Materials Science (EMAT)  
University of Antwerp  
Groenenborgerlaan 171, 2020 Antwerp, Belgium  
E-mail: Nick.Schryvers@uantwerpen.be

G. F. Nataf  
Materials Research and Technology Department  
Luxembourg Institute of Science and Technology  
41 rue du Brill L-4422, Belvaux, Luxembourg

G. F. Nataf  
SPEC, CEA, CNRS  
Université Paris-Saclay  
CEA Saclay  
91191 Gif-sur-Yvette, France

Dr. L. Jones  
Department of Materials  
University of Oxford  
Parks Road, Oxford OX1 3PH, UK

Prof. A. M. Abakumov  
Center for Electrochemical Energy Storage  
Skolkovo Institute of Science and Technology  
Nobelya str. 3, 143026 Moscow, Russia

Prof. E. K. H. Salje  
Department of Earth Sciences  
University of Cambridge  
Downing Street, Cambridge CB1 3EQ, UK



DOI: 10.1002/adfm.201603489

displacements of the oxygen cages.<sup>[30,31]</sup> The crystallographic properties and energetics of domain walls in  $\text{LiNbO}_3$  have been described in great detail in refs. [31] and, [32] we refer the reader to the excellent review in ref. [31] for further details. In the present paper, we confirm the presence of domain wall meanders even in  $\text{LiNbO}_3$  without engineered inclined walls and demonstrate, for the first time, that head-to-head configurations exist in a nominally “straight” domain wall. This observation confirms that local charges occur inside domain walls in  $\text{LiNbO}_3$ .

## 2. Results and Discussion

$\text{LiNbO}_3$  is an electron beam-sensitive material. Therefore, both the transmission electron microscopy (TEM) specimen preparation and the high angle annular dark field scanning transmission electron microscopy (HAADF-STEM) image acquisition were optimized in order to obtain most reliable TEM data. The most optimal focused ion beam (FIB) lamella (Figure 1b) had a thickness of about 70 nm (estimated using electron energy loss spectroscopy), which is a compromise between the electron transparency and the ion-beam damage during the sample preparation. The HAADF-STEM data were collected along the  $[1\bar{1}00]$  direction, as a time series of 49 frames with a very short acquisition time of 2.5 s per frame. This mode significantly reduces the dose rate, improving the stability of the material under the electron beam, and minimizes the effect of mechanical instabilities of the sample during the experiment. In all other experimental approaches, radiation damage became too severe too fast to allow for any useful quantitative measurements.

The acquired data were processed using the Smart Align software package.<sup>[33]</sup> First, all the frames were aligned with respect to each other to compensate for the mechanical drift during the acquisition. Then, each frame was individually corrected for the scan distortions. In the end, the frames were combined into a single image with improved signal-to-noise ratio and minimized scan and drift distortions. A representative fragment of the averaged image is shown in Figure 2a. The position of the ferroelectric domain wall is marked with a white arrow, and can be seen as a strip with a slightly lower intensity. Also, it creates a weak ripple in the rows of white dots when looking at this image along a grazing incidence from left to right. In the HAADF-STEM images, the signal is dependent on the chemical composition of the projected atomic columns and scales as  $I \sim Z^{1.6-1.9}$ , where  $Z$  is an average atomic number. Therefore, in the  $[1\bar{1}00]$  HAADF-STEM images of  $\text{LiNbO}_3$ , the projected Nb-Li ( $Z[\text{Nb}] = 41$ ,  $Z[\text{Li}] = 3$ ) columns appear as bright dots arranged into a rectangular pattern, while the O ( $Z[\text{O}] = 8$ ) columns are not visible. In the following the Nb-Li columns are referred to as Nb columns since simulations have shown that, as can be expected, the Li atoms are too light to cause any visible effect in the imaging.

To analyze the Nb atomic displacements at the ferroelectric domain wall, the projected 2D coordinates of the Nb columns in the averaged  $[1\bar{1}00]$  HAADF-STEM image were determined using statistical parameter estimation theory.<sup>[34-36]</sup> The image was fitted with a parametric model in which the intensity distribution of each atomic column in the image is described as a

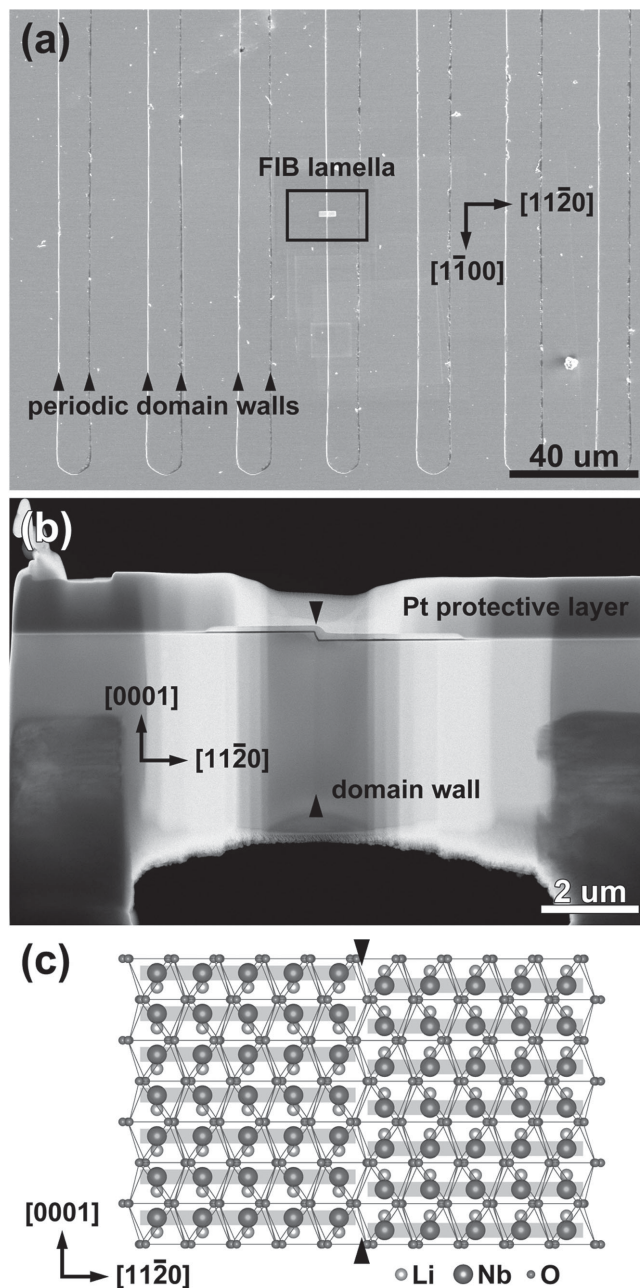


**Figure 1.** a) Overview scanning electron microscopy (SEM) image of the investigated  $\text{LiNbO}_3$  crystal viewed normal to the surface, i.e., along the  $[0001]$  direction. Induced domain walls appear as a set of periodic parallel lines. The site where the FIB specimen was extracted can be seen as a bright narrow strip of the Pt protective layer. b) Low magnification HAADF-STEM image of an optimized FIB lamella, viewed along the  $[1\bar{1}00]$  direction. The domain wall (marked with arrowheads) can be recognized as a thin straight line of weaker intensity running along the  $[0001]$  direction and located right under the surface step. c) Idealized schematic illustration of the domain wall, assuming the oxygen sublattice to remain unchanged when crossing the domain wall. Rows of Nb atomic columns are highlighted with gray stripes.

Gaussian function, peaked at the column position. The parameters of this model, including the positions, height, and width of the Gaussian peaks, were determined using the least-square



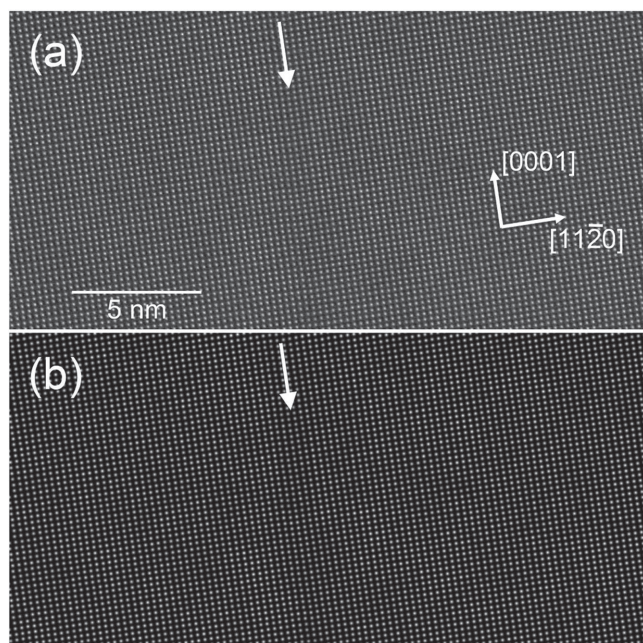


**Figure 2.** a) The  $[1\bar{1}00]$  HAADF-STEM image of the ferroelectric domain wall area in the  $\text{LiNbO}_3$  sample, averaged over 49 frames and corrected for the drift and scan distortions. b) The fitted model of the HAADF-STEM image. The arrows indicate the direction and location of the interface.

estimator. The refined model is shown in Figure 2b, where the position of the domain wall is again indicated with a white arrow.

For the determination of the Nb positions, we assume that the ferroelectric domain wall does not change the anion sublattice of the structure, but inverts the ferroelectric displacements of the Nb cations. The inverted Li positions cannot be extracted from the images because the Li atomic scattering factor is much smaller than Nb so that all observed displacements are nominally related to Nb. The following procedure was employed to identify the pattern of cation displacements and the sideways displacements, if any, of the domain wall along the  $[11\bar{2}0]$  direction. First, a region of 90 atomic rows was selected along the  $[0001]$  direction, each of which measuring 59 atomic columns along the  $[11\bar{2}0]$  direction (this region is the shaded rectangle in Figure 3a). Then, for each row of 59 columns, two reference lines were fitted by linear regression, using the coordinates of the 15 Nb columns at both ends of the row on either side of the wall (green lines in Figure 3b). In this fit, the slope of the reference lines for a given row at both sides of the domain wall was restricted to be the same, whereas the intercept with the interface was allowed to vary. The slopes for different atomic rows were not restricted.

To calculate the ferroelectric displacements of the Nb atoms, a base line for every  $[11\bar{2}0]$  atomic row was then defined midway both reference lines (red line in Figure 3b, which has the same slope as both fitted green reference lines). The red line

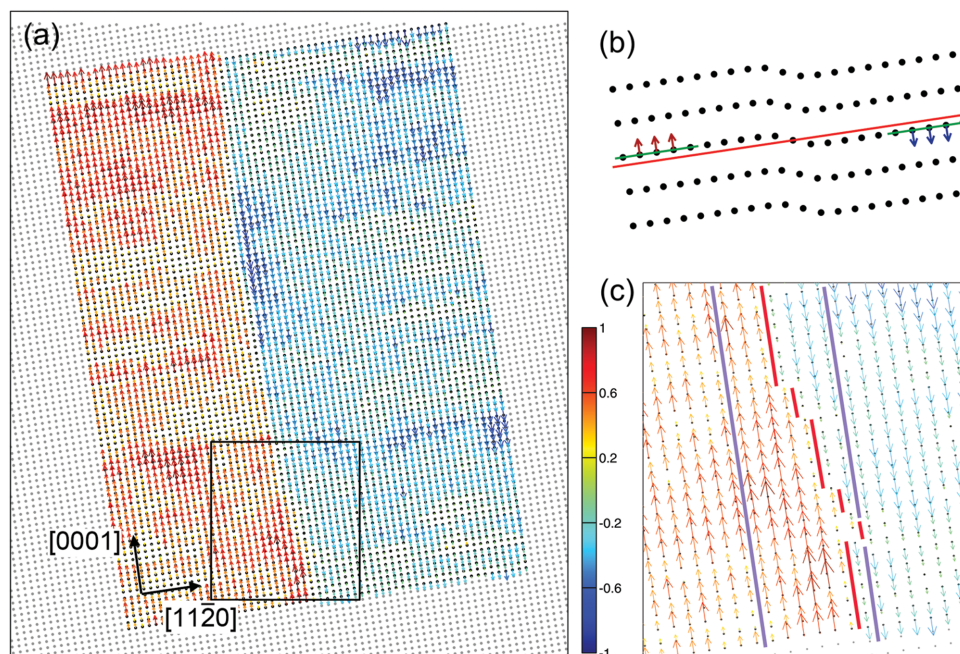


**Figure 3.** a) The analyzed region of 90 reference atomic rows: grey dots correspond to the fitted atom column positions, red and blue arrows indicate the displacement of the fitted atomic positions with respect to the base line and pointing in the direction of the displacement (the larger the displacement, the darker and longer the arrow). b) Schematic (stretched in the  $[0001]$  direction for clarity) showing green reference lines fitted to reference Nb columns in each ferroelectric domain and the red base line midway those reference lines. c) Enlargement of the squared area in (a), where now the straight domain wall segments are indicated in red. Purple lines indicate the transition region, where the Nb displacements are inverted (i.e., the overall width of the domain wall). Another sample image from a different part of the interface is shown in Figure S1 of the Supporting Information.

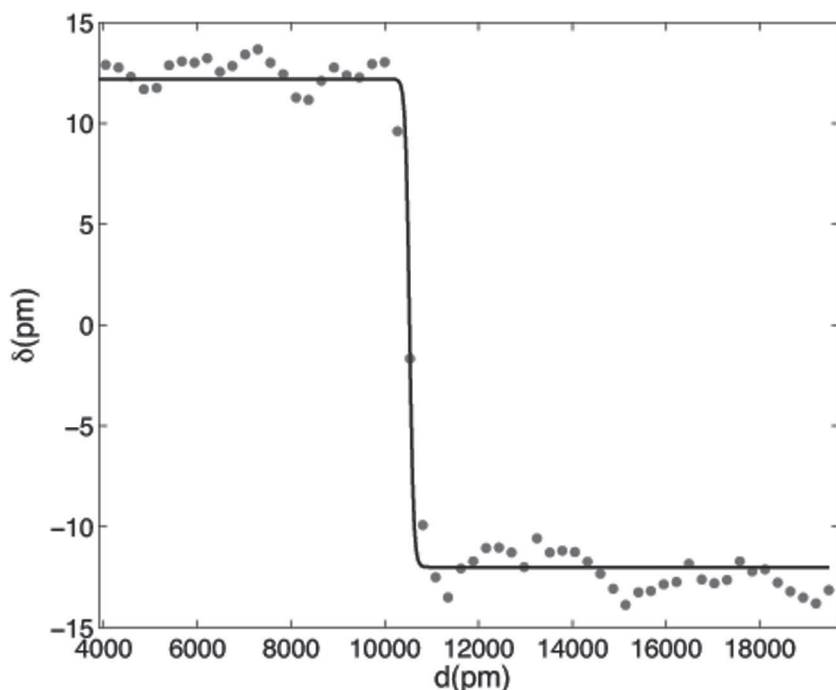


**Figure 4.** The master curve of Nb displacements in the analyzed region (dots) and the corresponding fitted parametric model (curve).

represents the approximate position of Nb in the paraelectric phase. Then, the Nb displacement from the red line for each column was calculated for each Nb column. This displacement represents the approximate ferroelectric shift of Nb. By design, this implies that we only measure the displacements of the Nb columns along the [0001] direction, i.e., parallel to the  $(11\bar{2}0)$  domain wall. In Figure 3, the displacements are represented with the vectors pointing in the direction of the displacement.

The location of the domain wall along the  $[11\bar{2}0]$  direction in a given row of Nb atomic columns can be determined as the point where the polar displacements of Nb columns change direction. The location points of the domain wall do not form perfectly straight lines along [0001], but meander back and forth along the  $[11\bar{2}0]$  direction. Nevertheless, straight segments of the domain wall can be identified (red lines in Figure 3c). The overall meanders and local kinks between the wall segments occur within a narrow region of about seven unit cells along the  $[11\bar{2}0]$  direction, represented by the purple full lines in Figure 3c. On a mesoscopic length scale, the domain wall is well confined to the  $(11\bar{2}0)$  plane.

Having quantified the off-center displacement of the Nb columns near the ferroelectric domain wall, the width of the wall in each of the 90 selected Nb rows was analyzed using a simple parametric model<sup>[37]</sup>

$$f(\beta_1, \beta_2, \beta_3, \beta_4) = \beta_1 + \beta_2 \tanh\left(\frac{x - \beta_3}{\beta_4}\right) \quad (1)$$

where  $x$  represents the coordinates of the fitted atomic columns along  $[11\bar{2}0]$  in a single Nb column row,  $\beta_1$  corresponds to the position of the domain wall midpoint along the [0001] direction, i.e., the base line of the atomic row (red line in Figure 3b),

$\beta_2$  corresponds to the distance between the base line and the corresponding reference lines,  $\beta_3$  denotes the position of the domain wall midpoint along  $[11\bar{2}0]$ , and  $\beta_4$  represents the half-width of the transition region of the domain wall along  $[11\bar{2}0]$ . In the model, the width of the domain wall corresponds to  $2\beta_4$  and it is independent of the actual location of the interface within the row ( $\beta_1$  values are given in the Supporting Information).

Analysis of the calculated widths of the domain walls for all 90 atomic rows demonstrates that there are two characteristic ranges of the wall widths (see the corresponding histogram in Figure S2 in the Supporting Information). Most of the rows have a very narrow width of the domain wall, showing a step-like behavior of Nb displacements. However, nine rows show much wider widths of up to about 20 unit cells, which could be due to a meandering of the interface along the viewing direction.

Considering only the atomic rows that demonstrate a sharp transition in the Nb off-center displacements across the domain wall, an average wall width of  $174 \pm 33$  pm was calculated. Alternatively, an averaged

master curve for the Nb displacements in the entire region of interest was constructed. The atomic rows were first aligned with respect to each other along the  $[11\bar{2}0]$  direction, to compensate for the side-ways meanders in the position of the wall. The obtained master curve for the whole region is shown in Figure 4. The dots correspond to the averaged atomic column positions for a given row. The curve represents the fitted parametric model, which also estimates the averaged domain wall width as 174 pm. The master curve illustrates that on average the domain wall is associated with sharp transitions in the polar displacements of the Nb atoms, accounting for just three unit cells along the  $[11\bar{2}0]$  direction. Besides, the average displacements of the first atoms on either side of the wall from the base line are estimated as 9.4 pm, which is only slightly lower than the average value of 12.38 pm for the rest of the row and confirms the sharpness of the averaged interface. In a recent work, Wei et al. found a width of seven pseudocubic unit cells and an averaged lead atom displacement of 8 pm at antiphase boundaries in  $\text{PbZrO}_3$  using negative spherical aberration imaging and averaging over selected atomic rows, but without using parameter estimation theory.<sup>[38]</sup>

The main structural features of the wall in Figure 3c are the kinks of the displacements by one unit cell. While the overall direction is well defined, one could define the mesoscopic wall width as the distance between the two purple limiting lines (seven unit cells). Over rather long distances, the wall position does not fluctuate beyond this corridor. This situation is very different on a truly atomic scale where kinks with a step of one unit cell are rather common. Only these kinks produce local charges whenever two dipoles with opposite directions meet at a kink of the wall. These kinks can have a high density with five kinks over 26 unit cells along the [0001] direction while they are



less common in other parts of the sample. The total histogram of the length of the complete segments between two successive kinks and along the [0001] direction is given in Figure S3 (Supporting Information). Short segments (less than five rows) appear about twice as much as long segments (greater than five rows), the average segment length being between five and six rows, which is a high density so the hopping energy is expected to be small. If all kinks in the section seen in Figure 3c were oriented in the same direction, the wall would be inclined by a fraction of degree. Such walls were shown to exhibit Cherenkov second harmonic generation (CSHG) and various fine structures of domain walls have been made visible optically.<sup>[17,39,40]</sup>

While the macroscopic wall inclination is strictly zero, the local inclinations and hence the number of kinks is large in our sample, which corresponds to the predominantly short segments as seen from Figure S3 (Supporting Information). This implies that the local wall conductivity (hopping) is large, but we do not expect large distance electronic transport because straight wall segments act as insulators between the kink-rich regions. This picture of local electronic resonances was advocated previously and our results fully support these findings.<sup>[27,41]</sup> Our results are also in agreement with the lack of conductivity of domain walls with a macroscopic inclination of zero.<sup>[16]</sup> Furthermore, the presence of a large number of kinks means that the domain wall is a rough interface and will sensibly affect the CSHG signal.

From the pairs of reference lines for each  $[11\bar{2}0]$  row of atomic columns in Figure 3, the average shift between the Nb atoms across the domain wall equals 25.0 pm with a standard error of 1.1 pm (i.e., the distance between the stripes of  $[11\bar{2}0]$  Nb rows along the [0001] direction in Figure 1c). This value is about half of the expected value of ca. 55 pm calculated from the crystallographic bulk data of  $\text{LiNbO}_3$  (see Table S1 in the Supporting Information). However, the spontaneous polarization and hence the Nb shift of 24 pm in the TEM sample is that of a thin film prepared by FIB, so it can be expected to be reduced with respect to the bulk value. This effect may be a genuine size effect or related to strain and topological disorder along the beam direction, which could also result in the heterogeneities in the displacements as seen away from the domain wall in Figure 3a. Nevertheless, all topological features of the domain wall appear to be the same as in bulk samples. To further test whether the patches of small and large displacements visible in Figure 3 are due to heterogeneous strain effects, the Nb shifts with respect to the position extrapolated from the four nearest neighbor sites were calculated.<sup>[42]</sup> This does indeed average the strain variable as seen in Figure S4 (Supporting Information) and thus largely eliminates the heterogeneities.

The agreement with findings of optical and conductivity investigations lead to a follow up question: to which extent are the local kinks stable or do they represent unstable states which change in time? To investigate such possible dynamics of the observed ferroelectric domain, the image processing and data analysis procedure described above were also performed on smaller sets of data, i.e., on the HAADF-STEM images averaged over the first 24 and last 24 frames. Taking precision ranges into account, in about 90% of the rows the measured position of the interface did not move between the first 24 and last 24 frames (Figure S5, Supporting Information). Some of

the rows that showed a changing location of the interface are located in areas where the interface width (i.e.,  $2\beta_1$ ) was found to be about 20 unit cells (cfr. Figure S2, Supporting Information), but others were located at rows with a sharp interface. At present, it is thus unclear whether or not this observation is due to any dynamics of the system within the timeframe of 125 s of the experiment, but it appears possible that such instabilities exist.<sup>[43]</sup> It may be a possible next step toward the identification of such time dependences to make use of the CSHG radiation as function of time.

### 3. Conclusions

We have shown that ferroelectric domain walls in  $\text{LiNbO}_3$  follow, within experimental resolution, the predictions for  $180^\circ$  walls. Even for equilibrated walls, we find that the wall locally meanders yielding local wall directions inclined with respect to the ferroelectric polarization. These meanders generate kinks and dipolar configurations where the ferroelectric dipoles are oriented head-to-head or tail-to-tail. These configurations necessarily induce local charges, which do not destabilize the overall wall configuration.

### 4. Experimental Section

The original material was a congruent periodically poled  $\text{LiNbO}_3$  (PPLNb<sup>[29]</sup>) single crystal, commercially available from EQ Photonics GmbH. It had been poled at room temperature, with an experimental arrangement similar to the one described by Myers et al.<sup>[44]</sup> To identify the position of the domain wall, the sample was subsequently etched with hydrogen fluoride (HF), resulting in a height difference between adjacent domains (Figure 1a,b).<sup>[45]</sup> These preparative steps were performed by the supplier.

The pattern of atomic displacements at the ferroelectric domain wall in  $\text{LiNbO}_3$  was observed using HAADF-STEM. The TEM specimens were prepared using FIB with a dual-beam FEI Helios Nanolab 650 instrument. To minimize detrimental effects of the FIB sample preparation, the sample was protected by two layers of Pt-deposition, first electron-beam assisted at 5 kV, 3.2 nA and second ion-beam assisted at 30 kV and 0.23 nA to avoid surface damage. The initial thinning was done at various settings between 8 and 30 kV, while the final polishing was done at low ion-beam energy (2 kV, 23 pA). The thickness of the samples was optimized by successive back-and-forth FIB thinning and TEM observation runs and the analyzed region was selected close to the sample surface, i.e., immediately beneath the Pt protection layer where typically the least amount of damage was expected, as confirmed by the lack of a clear Ga signal in STEM-EDX (energy dispersive X-ray analysis).

FIB lamellae were cut along the [0001] crystallographic direction (i.e., normal to the crystal surface) and perpendicular to the domain wall (Figure 1a). In this orientation, when analyzed with TEM, the samples provided a clear view of the atomic structure along the  $[1\bar{1}00]$  crystallographic direction, i.e., parallel to the  $(11\bar{2}0)$  domain wall. HAADF-STEM images were acquired with an FEI Titan<sup>3</sup> 60–300 probe aberration corrected microscope operated at 300 kV, with a probe semiconvergence angle of 21 mrad, a probe current of 40 pA, and the inner angle of the annular detector set at 58 mrad.

### Supporting Information

Supporting Information is available from the Wiley Online Library or from the author.

## Acknowledgements

J.G. acknowledges the support from the Research Foundation Flanders (FWO, Belgium) through various project fundings (G.0368.15N, G.0369.15N, and G.0374.13N), as well as the financial support from the European Union Seventh Framework Program (FP7/2007–2013) under Grant agreement no. 312483 (ESTEEM2). The authors thank J. Hadermann for useful suggestions on the interpretation of the HAADF-STEM images. E.K.H.S. thanks the EPSRC (EP/K009702/1) and the Leverhulme Trust (EM-2016-004) for support. G.F.N. thanks the National Research Fund, Luxembourg (FNR/P12/4853155/Kreisel) for support.

Received: July 11, 2016

Revised: August 18, 2016

Published online: September 16, 2016

- [1] E. K. H. Salje, *ChemPhysChem* **2010**, *11*, 940.
- [2] J. Seidel, P. Maksymovych, Y. Batra, A. Katan, S.-Y. Yang, Q. He, A. P. Baddorf, S. V. Kalinin, C.-H. Yang, J.-C. Yang, Y.-H. Chu, E. K. H. Salje, H. Wormeester, M. Salmeron, R. Ramesh, *Phys. Rev. Lett.* **2010**, *105*, 197603.
- [3] S. Farokhipoor, B. Noheda, *Phys. Rev. Lett.* **2011**, *107*, 127601.
- [4] O. Diéguez, P. Aguado-Puente, J. Junquera, J. Íñiguez, *Phys. Rev. B* **2013**, *87*, 024102.
- [5] J. Guyonnet, I. Gaponenko, S. Gariglio, P. Paruch, *Adv. Mater.* **2011**, *23*, 5377.
- [6] A. Aird, E. K. H. Salje, *J. Phys.: Condens. Matter* **1998**, *10*, L377.
- [7] Y. Kim, M. Alexe, E. K. H. Salje, *Appl. Phys. Lett.* **2010**, *96*, 032904.
- [8] H. Yokota, H. Usami, R. Haumont, P. Hicher, J. Kaneshiro, E. K. H. Salje, Y. Uesu, *Phys. Rev. B* **2014**, *89*, 144109.
- [9] S. Van Aert, S. Turner, R. Delville, D. Schryvers, G. Van Tendeloo, E. K. H. Salje, *Adv. Mater.* **2012**, *24*, 523.
- [10] E. K. H. Salje, O. Aktas, M. A. Carpenter, V. V. Laguta, J. F. Scott, *Phys. Rev. Lett.* **2013**, *111*, 247603.
- [11] J. F. Scott, E. K. H. Salje, M. A. Carpenter, *Phys. Rev. Lett.* **2012**, *109*, 187601.
- [12] S. Farokhipoor, C. Magén, S. Venkatesan, J. Íñiguez, C. J. M. Daumont, D. Rubi, E. Snoeck, M. Mostovoy, C. de Graaf, A. Müller, M. Döblinger, C. Scheu, B. Noheda, *Nature* **2014**, *515*, 379.
- [13] A. Y. Borisevich, O. S. Ovchinnikov, H. Jung Chang, M. P. Oxley, P. Yu, J. Seidel, E. A. Eliseev, A. N. Morozovska, R. Ramesh, S. J. Pennycook, S. V. Kalinin, *ACS Nano* **2010**, *4*, 6071.
- [14] J. Seidel, L. W. Martin, Q. He, Q. Zhan, Y.-H. Chu, A. Rother, M. E. Hawkrige, P. Maksymovych, P. Yu, M. Gajek, N. Balke, S. V. Kalinin, S. Gemming, F. Wang, G. Catalan, J. F. Scott, N. A. Spaldin, J. Orenstein, R. Ramesh, *Nat. Mater.* **2009**, *8*, 229.
- [15] M. Schröder, A. Haußmann, A. Thiessen, E. Soergel, T. Woike, L. M. Eng, *Adv. Funct. Mater.* **2012**, *22*, 3936.
- [16] M. Schröder, X. Chen, A. Haußmann, A. Thiessen, J. Poppe, D. A. Bonnell, L. M. Eng, *Mater. Res. Express* **2014**, *1*, 035012.
- [17] T. Kämpfe, P. Reichenbach, M. Schröder, A. Haußmann, L. M. Eng, T. Woike, E. Soergel, *Phys. Rev. B* **2014**, *89*, 035314.
- [18] E. A. Eliseev, A. N. Morozovska, G. S. Svehnikov, V. Gopalan, V. Y. Shur, *Phys. Rev. B* **2011**, *83*, 235313.
- [19] C.-L. Jia, S.-B. Mi, K. Urban, I. Vrejoiu, M. Alexe, D. Hesse, *Nat. Mater.* **2008**, *7*, 57.
- [20] V. Aristov, L. Kokhanchik, *Ferroelectrics* **1992**, *126*, 353.
- [21] V. V. Aristov, L. S. Kokhanchik, Y. I. Voronovskii, *Phys. Status Solidi* **1984**, *86*, 133.
- [22] L. S. Kokhanchik, *Micron* **2009**, *40*, 41.
- [23] G. Catalan, J. Seidel, R. Ramesh, J. F. Scott, *Rev. Mod. Phys.* **2012**, *84*, 119.
- [24] G. F. Nataf, O. Aktas, T. Granzow, E. K. H. Salje, *J. Phys.: Condens. Matter* **2016**, *28*, 015901.
- [25] H. Xu, D. Lee, J. He, S. Sinnott, V. Gopalan, V. Dierolf, S. Phillpot, *Phys. Rev. B* **2008**, *78*, 174103.
- [26] S. C. Abrahams, P. Marsh, *Acta Crystallogr., Sect. B: Struct. Sci.* **1986**, *42*, 61.
- [27] P. Lerner, C. Legras, J. P. Dumas, *J. Cryst. Growth* **1968**, *3*, 231.
- [28] H. Xu, D. Lee, S. B. Sinnott, V. Gopalan, V. Dierolf, S. R. Phillpot, *IOP Conf. Ser.: Mater. Sci. Eng.* **2010**, *15*, 012003.
- [29] G. Stone, D. Lee, H. Xu, S. R. Phillpot, V. Dierolf, *Appl. Phys. Lett.* **2013**, *102*, 042905.
- [30] K. Shapovalov, P. V. Yudin, A. K. Tagantsev, E. A. Eliseev, A. N. Morozovska, N. Setter, *Phys. Rev. Lett.* **2014**, *113*, 207601.
- [31] V. Gopalan, V. Dierolf, D. A. Scrymgeour, *Annu. Rev. Mater. Res.* **2007**, *37*, 449.
- [32] L. Donghua, X. Haixuan, D. Volkmar, V. Gopalan, S. R. Phillpot, *Phys. Rev. B* **2010**, *82*, 014104.
- [33] L. Jones, H. Yang, T. Pennycook, M. Marshall, S. Van Aert, N. Browning, M. Castell, P. D. Nellist, *Adv. Struct. Chem. Imaging* **2015**, *1*, 8.
- [34] A. J. den Dekker, J. Gonnissen, A. De Backer, J. Sijbers, S. Van Aert, *Ultramicroscopy* **2013**, *134*, 34.
- [35] A. J. den Dekker, S. Van Aert, A. van den Bos, D. Van Dyck, *Ultramicroscopy* **2005**, *104*, 83.
- [36] S. Van Aert, J. Verbeeck, R. Erni, S. Bals, M. Luysberg, D. Van Dyck, G. Van Tendeloo, *Ultramicroscopy* **2009**, *109*, 1236.
- [37] E. K. H. Salje, *Annu. Rev. Mater. Res.* **2012**, *42*, 265.
- [38] X.-K. Wei, A. K. Tagantsev, A. Kvasov, K. Roleder, C.-L. Jia, N. Setter, *Nat. Commun.* **2014**, *5*, 3031.
- [39] Y. Sheng, A. Best, H. J. Butt, W. Krolikowski, A. Arie, K. Koynov, *Opt. Express* **2010**, *18*, 16539.
- [40] T. Kämpfe, P. Reichenbach, A. Haußmann, T. Woike, E. Soergel, L. M. Eng, *Appl. Phys. Lett.* **2015**, *107*, 152905.
- [41] A. Tselev, P. Yu, Y. Cao, L. R. Dedon, L. W. Martin, S. V. Kalinin, P. Maksymovych, *Nat. Commun.* **2016**, *7*, 11630.
- [42] T. Jach, S. Kim, V. Gopalan, S. Durbin, D. Bright, *Phys. Rev. B* **2004**, *69*, 64113.
- [43] E. K. H. Salje, X. Wang, X. Ding, J. Sun, *Phys. Rev. B* **2014**, *90*, 064103.
- [44] L. E. Myers, R. C. Eckardt, M. M. Fejer, R. L. Byer, W. R. Bosenberg, J. W. Pierce, *J. Opt. Soc. Am. B* **1995**, *12*, 2102.
- [45] C. L. Sones, S. Mailis, W. S. Brocklesby, R. W. Eason, J. R. Owen, *J. Mater. Chem.* **2002**, *12*, 295.